Numerical determination of pressure-dependent effective thermal conductivity in Berea sandstone

Mirko Siegert[1,3*], Marcel Gurris[1], Claudia Finger[2] and Erik H. Saenger[1,2,3]

[1]*Bochum University of Applied Sciences, Am Hochschulcampus 1, Bochum, 44801, Germany,* [2]*Fraunhofer IEG, Am Hochschulcampus 1, Bochum, 44801, Germany, and* [3]*Ruhr-University Bochum, Universitaetstrasse 150, Bochum, 44801, Germany*

ABSTRACT

In this paper, the methods of digital rock physics are applied to determine pressure-dependent effective thermal conductivity in rock samples. Simulations are performed with an in-house three-dimensional finite volume code. In the first step, four numerical models are derived from a given tomographic scan of Berea sandstone. Consequently, simulations of the thermal conductivity at ambient conditions are performed and validated with experimental data. In a second step, a new workflow for the determination of the pressure-dependent thermal conductivity in rock samples is elaborated, tested and calibrated. Results originating from the derived workflow show very good agreement with experimental data.

Key words: Numerical study, Pressure-dependent thermal conductivity, Digital rock physics, Tomography.

1 INTRODUCTION

For the technical use of geothermal applications, detailed knowledge of the thermal conductivity of the underlying rock formation is of great importance. Typical examples are basin modelling for the prediction of hydrocarbon maturation (Chekhonin *et al.*, 2019), analysis of geothermal reservoirs for energy production or storage (Sipio *et al.*, 2013) and finding suitable locations for nuclear waste disposal (Mirkovich and Soles, 1978).

In general, the thermal conductivity of rocks can be understood as a macroscopic quantity, which mainly depends on the material composition as well as its pore structure. Due to the depth-dependent geothermal and geobaric gradient (Lowrie and Fichtner, 2020; Tiab and Donaldson, 2016), it is also reasonable to consider temperature and pressure effects.

The determination of thermal conductivity of rocks can be performed experimentally or numerically. A large collection of experimental data can be found in Cermak and Rybach (1982), Horai (1971), Desai *et al.* (1974) and Clauser and

Huenges (2013). Experimental studies with an increased focus on temperature and pressure effects can be found in Woodside and Messmer (1961), Abdulagatov *et al.* (2006) and Lin *et al.* (2011). A good summary of numerical approaches is given in Wang and Pan (2008).

Concerning the above-mentioned example of basin modelling, Hicks *et al.* (2012) and Blackwell and Steele (1989) have pointed out that the quality of the simulations might be strongly dependent on the input values for thermal conductivity. If no experimental data are available, one relies on numerical approaches. One such approach is digital rock physics (DRP). In DRP, a three-dimensional model of the underlying microstructure, based on a tomographic scan of the investigated rock, is created. This model is used as an input for a numerical solver. From the results of the numerical simulation, the macroscopic quantities can be determined. Examples of this approach can be found in Qin *et al.* (2020), Do and Hoxha (2013), Yang *et al.* (2019), Jones and Pascal (1995) and Petrasch *et al.* (2008). Although a wide variety of DRP models for the determination of thermal conductivity are available, to this date there are no models that mimic the influence of pressure.
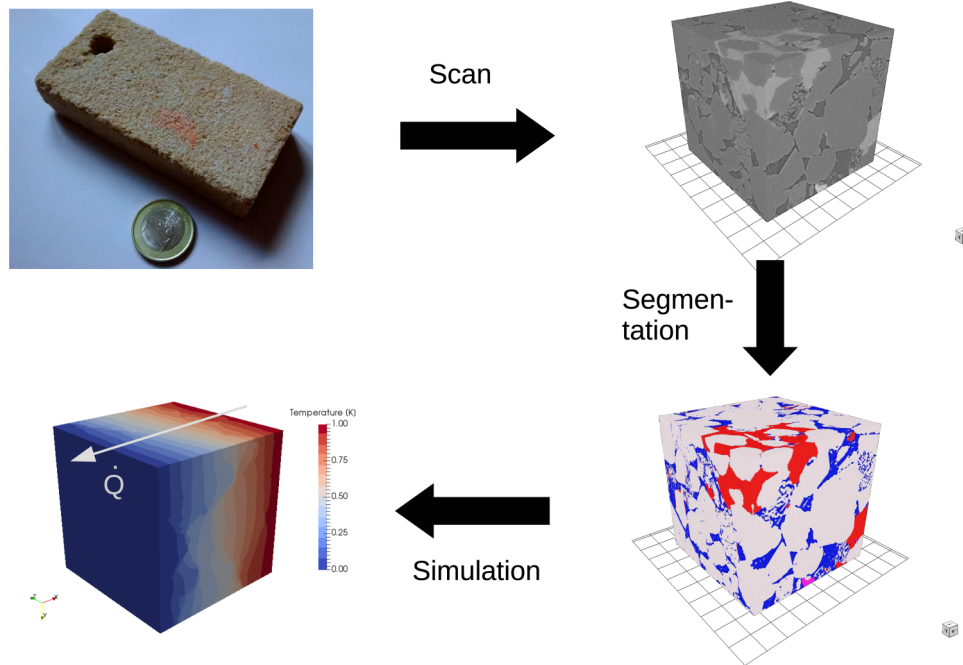
Figure 1 Typical workflow of the digital rock physics approach.

The main objective of this study is the development of a new DRP workflow for the determination of pressure-dependent thermal conductivity based on the microstructure of rock samples. Generally, our model is based on the ideas of Quintal *et al*. (2011), Madonna *et al*. (2012) and Saenger *et al*. (2016). In these publications, a DRP workflow for the determination of pressure-dependent elasticity was discussed and successfully tested. In particular, the model is based on the assumption that the contact area between the individual grains of the rock plays a decisive role. By applying pressure, the contact area is increased and the macroscopic property under consideration changes.

Pimienta *et al*. (2014) observed that the pressure-dependent elasticity and thermal conductivity of sandstones might behave similarly. Based on this observation, we attempt to transfer the above-mentioned elasticity approach to the modelling of pressure-dependent thermal conductivity. For the validation of the model, we restrict ourselves to sedimentary rocks, in our case Berea sandstone. Simulation results are compared with experimental data of up to 50 MPa. Additionally, to optimize the agreement between simulation and experiment, a physically motivated calibration process is presented and tested.

The paper is divided into four parts. We start with a discussion of the computational approach and present the rock sample studied here. Building on this, we carry out our in-

vestigations. Thermal conductivities at ambient conditions are simulated. The results are validated and compared with experimental data. Furthermore, the numerical error is analysed. Different numerical approaches are used, and mesh refinement studies are performed. Subsequently, simulations for the pressure-dependent thermal conductivity are carried out and tested. The paper ends with a discussion of the results.

2 METHOD

We follow a workflow commonly used in DRP to simulate effective properties of rock samples. As a starting point, a tomographic scan of a rock sample is taken. The resulting greyscale image is segmented to determine all phases of the sample, for example minerals and pore space. Each phase is prescribed with a given material property and loaded into a numerical solver. The related governing equations will be solved, and the effective property can be calculated. An overview of this workflow is given in Figure 1. In our case, we want to determine the effective thermal conductivity of rock samples. All simulations will be performed with our in-house code (Siegert *et al*., 2021). Assuming a steady heatflow solely influenced by pure heat conduction using Fourier's law (Fourier, 1822), the governing equation reads as follows:
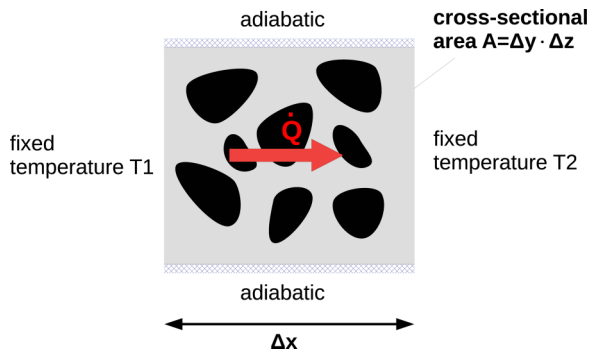
$$-\nabla(k\nabla T) = q, \tag{1}$$

Figure 2 Schematic representation of boundary conditions in two dimensions.

Figure 3 Pore size distributions of the Berea sandstone samples used in Madonna *et al.* (2013) and Lin *et al.* (2011).

with *k* is thermal conductivity and *q* is heat sources. The temperature field being solved for is represented by the variable *T*. This equation is solved numerically using the finite volume method. The corresponding numerical mesh is directly derived from the segmented tomographic scan. Every voxel is translated to a control volume, and the corresponding thermal conductivity is assigned.

During the simulation process, equation (1) is discretized and evaluated for every single control volume. The resulting linear system of equations is solved with an iterative method. In particular, we use the conjugated gradients method (Hestenes and Stiefel, 1952). As a stopping criterion, the L1-residual is computed. Once the residual is below 10^{-10} simulations are terminated.

In general, all simulations are performed with cuboid meshes. Thus, modelling of directional dependencies is relatively straightforward. This is done by applying Dirichlet boundary conditions on two opposing sides, leading to a fixed temperature difference of $\Delta T = 1$ across the sample. The remaining sides are treated adiabatically with Neumann boundary conditions, that is, a zero gradient normal to the surface $\nabla T = 0$. The resulting temperature field will be used to calculate heat fluxes across both sides, which in turn can be used to predict the effective thermal conductivity in the direction of one given basis vector (see Fig. 2)

$$k = \frac{\dot{Q}\Delta x}{A\Delta T}, \tag{2}$$

with $\dot{Q}$ being the heat flux flowing through the sample, Δx the dimension of the sample parallel to the heat flux, A the cross-sectional area of the sample perpendicular to the heat flux and ΔT the applied temperature difference. Additional simulations for the two remaining pairs of opposing sides lead to the effective thermal conductivity in all basis vector directions, namely k_{xx}, k_{yy} and k_{zz}.
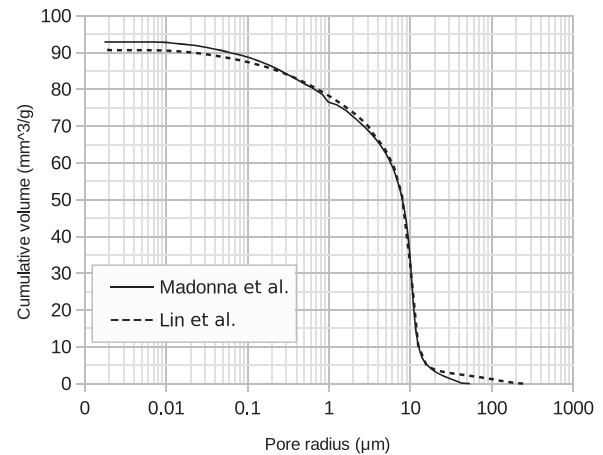
As shown in Patankar (1980) and Liu and Ma (2005), a crucial point in the numerical process is the averaging of the interfacial conductivity between two control volumes. Our solver supports two methods, namely the harmonic mean and the arithmetic mean. During this study, both approaches will be used, allowing to estimate the numerical error. For further information about these approaches, we refer to Maddix *et al.* (2018), Siegert *et al.* (2021), Kadioglu *et al.* (2008) and MacKinnon and Carey (1988).

2.1 Investigated rock sample

In the present study, the main object of investigation is the pressure-dependent thermal conductivity of Berea sandstone. Berea sandstone is a well-known reservoir rock, which has been extensively analysed in previous studies (Desai *et al.*, 1974).

Generally, all present simulations are based on the tomographic scan published by Madonna *et al.* (2013). The numerical results are compared with the experimental data published by Lin *et al.* (2011). Unfortunately, both investigations were carried out separately and are therefore not based on the exact same rock sample. However, in both studies mercury intrusion porosimetry measurements have been performed. The results are shown in Figure 3. As can be seen, the pore size distribution of both samples is very similar. In particular, the course of the intermediate pore radius interval between 0.1 and 20 μm is almost identical. Suggesting a comparison of both datasets is possible. The comparison of the total porosity with $\phi_{Lin} = 19.7\%$ and $\phi_{Madonna} \approx 20\%$ points in the same direction.
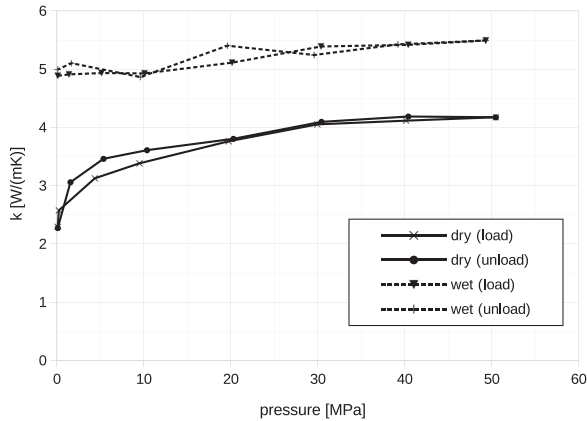
Figure 4 Pressure-dependent thermal conductivity of Berea sandstone, measured in its dry and wet state, originally published by Lin *et al.* (2011).

2.1.1 Experimental data

As mentioned earlier, the experimental data used in this study were originally published by Lin *et al.* (2011). In his work, Lin et al. analysed pressure-dependent thermal conductivity of four rock samples, one of which is Berea sandstone. All measurements were performed at room temperature and cover the pressure range from 0.1 to 50 MPa. The pressure is applied in a hydrostatic manner. Anisotropic effects are not analysed. In order to track hysteresis effects, each measurement run is divided into loading and unloading curves. Additionally, the sample was measured in its dry (pores are filled with air) and wet (pores are filled with ion-exchanged water) state. Each curve was measured multiple times, and the average was computed. Relative differences within one measuring point are below 2.4% for the dry sample and below 5.9% for the wet sample. The experimental data are shown in Figure 4.

As one can see, the thermal conductivity of the dry sample is always lower than the thermal conductivity of the wet sample. This observation is convincing since the thermal conductivity of water is roughly 23 times higher than the thermal conductivity of air under ambient conditions. Regarding the overall trend of the dry sample, the steep gradient at low pressures with the later almost linear behaviour stands out. This trend was also reported by Woodside and Messmer (1961) and is also observed for other material properties like elasticity and electric resistivity (Madonna *et al.*, 2012; Pimienta *et al.*, 2017). In contrast, the thermal conductivity of the wet sample seems to behave more or less linear for all pressure levels. At least, a steep gradient cannot be observed with the given measurement accuracy. Regarding hysteresis effects, both probes seem to show slight deviations between loading and unload-
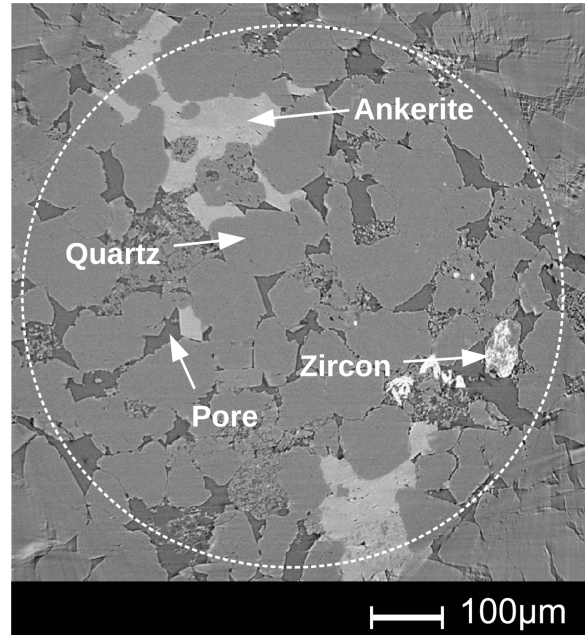

Figure 5 Representative slice of the tomographic image of the Berea sandstone sample, and four different phases are marked. The white circle separates the image artifacts, which mostly occur in the corners of the *xy*-plane, from the original image.

ing curves, though, the overall courses indicate that this might be related to a precision problem.

2.1.2 Tomographic data

The numerical model developed during this work is based on the tomographic data published by Madonna *et al.* (2013). In their work, Madonna et al. took tomographic scans of five different rock samples, one of which is Berea sandstone. The Berea-scan has been taken with a synchrotron radiation x-ray tomographic microscopy and a voxel resolution of 0.74 μm. The scanned sample is cubic in dimension with an edge length of 757.76 μm, resulting in a total voxel count of 1024^3. In order to analyse material composition, additional scanning electron microscope (SEM) images were taken. Madonna et al. concluded that five minerals appear in the SEM image, namely quartz, K-spar, clay, ankerite and zircon. Due to the poorer image quality of the tomographic scan, they assumed that only quartz, ankerite and zircon are distinguishable there (see Fig. 5).

Two points have to be taken into account when building the numerical model: First, as can be seen from Figure 5, image artefacts are present in the original tomographic dataset. These artefacts may cause issues during the segmentation
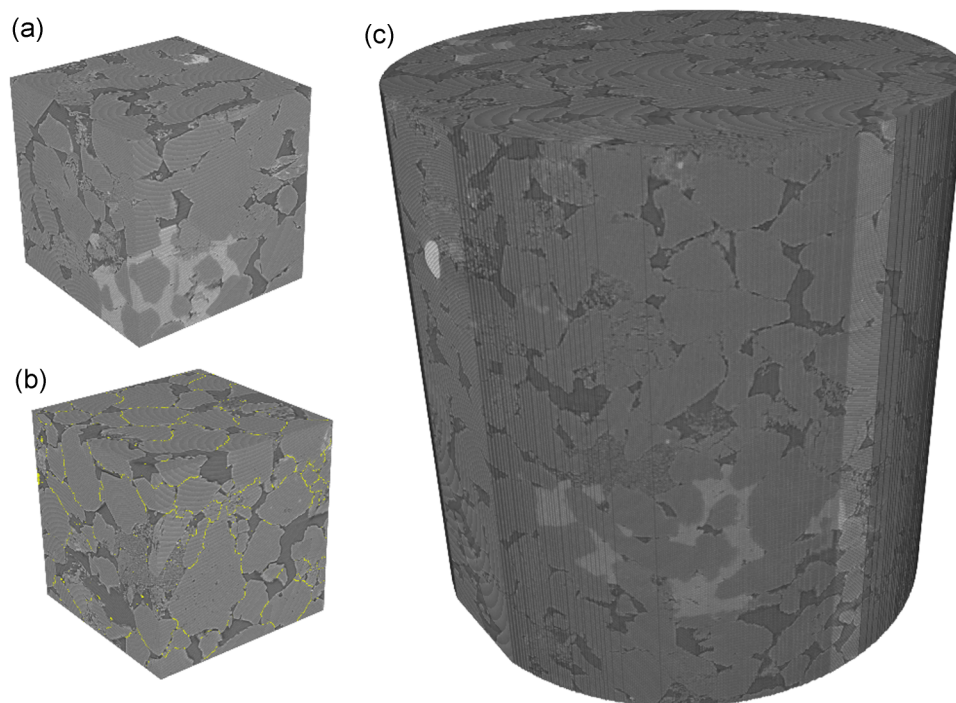
Figure 6 Graphical representation of all three subsamples, with the lightest grey representing zircon, second lightest grey ankerite, third lightest grey quartz, darkest grey pore and yellow contact phase. Sample 1 is placed on the top left, sample 2 on the bottom left and sample 3 on the right. The edge length of samples 1 and 2 is 296 μm, and the diameter of sample 3 is approximately 758 μm.

process and should be avoided for further analysis. Second, computational power is limited. With our current setup, a cluster with 240 CPU cores and 1.152 TB RAM, the maximum number of cells we can successfully handle is about 1200^3. Thus, the important step of mesh refinement and the associated numerical error analysis can only be done for sufficiently small datasets.

Taking these points into account, two subsamples from the original dataset are derived. The first subsample shall represent the material composition of the original dataset. It can be used to investigate the influence of the material composition during numerical simulations. The second sample was placed in such a way that mainly quartz is present. It forms the basis for the contact phase detection step using the watershed method (Beucher and Meyer, 2018) and will be used for the pressure-dependent simulations (see Section 4.1). In addition, a cylindrical subsample is cut out as a reference for the material composition of the entire sample, eliminating possible problems arising from the image artefacts mentioned above. This last sample is not used for simulation purposes.

Segmentation of all three subsamples is performed using the software Dragonfly (Object Research Systems, 2020). Artificial neural networks for the detection of each phase, namely

Table 1 Porosity and relative mineral composition of all three samples

	Porosity	$\frac{V_{quartz}}{V_{minerals}}$	$\frac{V_{ankerite}}{V_{minerals}}$	$\frac{V_{zircon}}{V_{minerals}}$	$\frac{V_{contact}}{V_{minerals}}$
Sample 1	16.24%	95.57%	4.08%	0.35%	0.00%
Sample 2	17.37%	97.86%	0.00%	0.00%	2.14%
Sample 3	17.31%	94.62%	4.93%	0.45%	0.00%

pore, quartz, ankerite and zircon, were trained. For the determination of the contact phase, the marker-controlled watershed algorithm of the software package ImagJ, MorphoLibJ plugin, is used (Legland *et al.*, 2016). The placement of the markers was carried out manually. A graphical representation of each sample is given in Figure 6, and the corresponding characteristics are shown in Table 1.

As can be seen, the general trend of the material composition is similar for all samples. All samples have a porosity of approximately 16–17.5%. In addition, quartz is the dominant mineral with a relative mineral content of at least 94%, followed by ankerite (approximately 5%) and zircon (approximately 0.5%). In comparison with the experimental data, it is also noticeable that the porosity of the samples is generally too low by about 3 percentage points. If the contact phase of
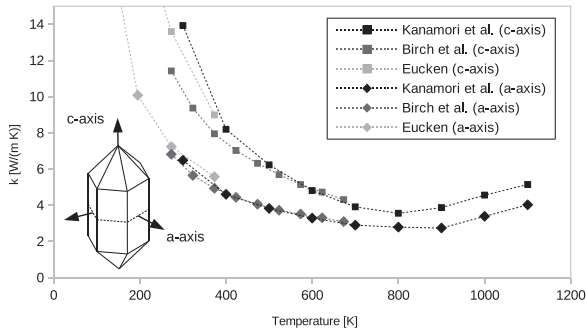
Figure 7 Temperature dependency of the thermal conductivity of quartz at ambient pressure (Eucken, 1911; Birch and Clark, 1940; Kanamori *et al.*, 1968).

sample 2 is added to the pore phase, the porosity is about 19%, and the deviation from the experimental data decreases accordingly.

2.2 Material Properties

To simulate the effective thermal conductivity in porous rocks, corresponding thermal conductivities must be assigned to each phase. In general, we assume that each phase can be properly modelled by the value of its related pure substance. As described above, to simulate the present Berea sandstone sample, thermal conductivities of five phases have to be known, namely air, water, quartz, ankerite and zircon. At large, these values depend on pressure and temperature. The determination of these values is not necessarily straightforward; a lack of available data, as well as anisotropic effects, might be a cause for that.

Experimental data for the present pore phase fluids are well documented and readily accessible. As shown by Span (2013) and Wagner and Kretzschmar (2013), thermal conductivity of air and water might be heavily dependent on temperature and pressure. However, it must be taken into account that in Lin's measurement setup, the pressure acts exclusively on the matrix structure of the rock sample, that is the pore pressure remains constant. Furthermore, the measurements are carried out at a constant temperature. Therefore, in the present case, pressure and temperature dependencies of the thermal conductivity of the pore phase can be neglected.

The determination of the thermal conductivity of the mineral phases is more demanding. Some insight into this problem will be discussed using the example of quartz. Its temperature dependence is given in Figure 7. As can be seen, the determination of the thermal conductivity is not unambiguous. On the one hand, a directional dependence on the thermal con-

Table 2 Thermal conductivity of the materials used in the present study, based on Span (2013), Wagner and Kretzschmar (2013) and Horai (1971)

	Air	Water	Quartz	Ankerite	Zircon
K [W m^{-1}K^{-1}]	0.026	0.61	7.69	5.51	4.54

ductivity can be observed. As a possible explanation for this anisotropy, the crystal structure of quartz can be referenced. Apparently, the thermal conductivity in the direction of the *c*-axis is generally greater than that of the *a*-axis. An approach widely used in the literature (Horai and Simmons, 1969; Pribnow and Umsonst, 1993) to average the directional dependence takes the weighting of the individual axes into account and results in

$$k_{\text{eff}} = \frac{1}{3}k_{\text{c-axis}} + \frac{2}{3}k_{\text{a-axis}}. \tag{3}$$

On the other hand, deviations occur between the individual measurement series. Especially in the range around 300 K, which is of particular interest in the present investigation, the largest differences are present. Due to this variation, the widely used literature value of 7.69 W m^{-1} K^{-1} was chosen (Horai, 1971; Cermak and Rybach, 1982; Clauser and Huenges, 2013).

Regarding the influence of pressure, we refer to the investigations of Beck *et al.* (1978). There, a relative increase in the thermal conductivity of up to 31% was observed for pressures in the range of 0.1 and 1950 MPa. Assuming a linear progression between these two measuring points, this means that for the pressure range of 0.1–50 MPa considered here, an expected relative change of less than 1% occurs. Consequently, pressure dependence is not taken into account.

In terms of data availability, quartz is considered an important material for technical applications, so its properties are well documented. In contrast, ankerite and zircon are less studied. Therefore, some assumptions to fill the gap of available data have to be made. First, we assume that the pressure dependence of ankerite and zircon is similar to that of quartz and can therefore be neglected. Second, to the best of our knowledge, no data are available for ankerite. Hence, it is assumed that the thermal conductivity of ankerite is similar to that of dolomite. This assumption is motivated by their corresponding chemical formulas, namely $Ca(Fe^{2+}, Mg, Mn^{2+})(CO_3)_2$ in the case of ankerite and $CaMg(CO_3)_2$ in the case of dolomite.

All thermal conductivities used in the present study are given in Table 2. All data are given at ambient conditions

(298.15 K, 0.1 MPa). As can be seen, the thermal conductivity of water is approximately one order of magnitude greater than that of air. In turn, the thermal conductivity of the minerals is about one order of magnitude greater than that of water.

3 THERMAL CONDUCTIVITY AT AMBIENT CONDITIONS

Within the scope of the first investigation, we restrict ourselves to the simulation of the thermal conductivity at ambient conditions, that is a temperature of 298.15 K and a pressure of 0.1 MPa. The investigation is divided into two parts. In a first step, basic trends are established using sample 1 and it is observed how well the numerical solution reproduces the experimental data. Subsequently, the influence of the individual samples is compared.

3.1 General numerical trend

This investigation will exclusively be performed with sample 1 (see Fig. 6). Within the numerical workflow, the following three points will be considered: First, the anisotropy of the thermal conductivity is taken into account. By adjusting the boundary conditions, the thermal conductivity of all three basis vector directions is calculated. Second, the influence of the averaging method at the cell interfaces is investigated. In particular, the harmonic and arithmetic mean are being used. Third, a mesh refinement study is performed. The simulations are executed on the base mesh with 400^3 cells as well as on a systematically refined mesh with $2^3 \times 400^3$ cells. These data will be used to extrapolate the analytical result, applying

$$k_{\text{ana}} \approx \frac{k_{\text{mesh},1} - k_{\text{mesh},2}\left(\frac{\Delta x_{\text{mesh},1}}{\Delta x_{\text{mesh},2}}\right)^p}{1 - \left(\frac{\Delta x_{\text{mesh},1}}{\Delta x_{\text{mesh},2}}\right)^p}, \tag{4}$$

with $k_{\text{mesh},i}$ is the numerical results, Δx_i is the edge length of the corresponding mesh cells and p is the order of convergence (Roache, 1997). Here, the observations published by Siegert *et al.* (2021) are considered, namely $p_b = 2$ for the harmonic mean and $p_a = 1$ for the arithmetic mean. A graphical representation of the numerical results is given in Figure 8 (consider dark grey areas only).

Overall, the simulated results lie above the experimental data. Regardless of the direction of the thermal conductivity, numerical results are approximately two times greater than the experimental data. Furthermore, it can be stated that the numerical results show a slight anisotropy, namely $k_{yy} > k_{zz} > k_{xx}$. Whereas the relative deviation of k_{xx} from the
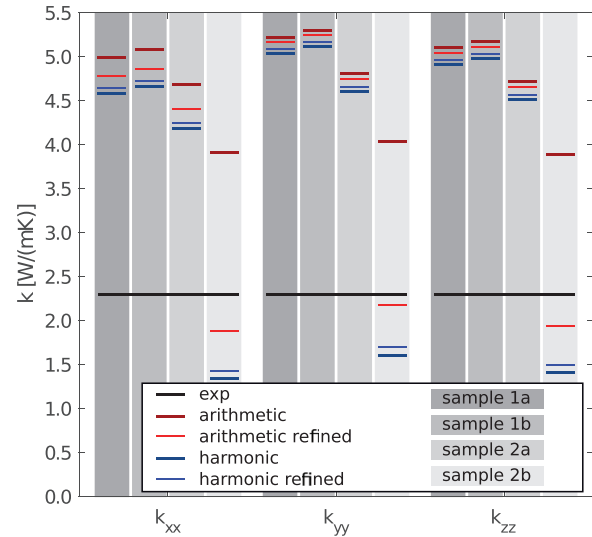
Figure 8 Anisotropic simulation results of all four samples in *x*, *y* and *z*-direction, and experimental data are given as a reference (black line). The dark grey area represents sample 1a, third lightest area sample 1b, second lightest area sample 2a and lightest area sample 2b. Results of the arithmetic mean are given in red, with light red being the results of the refined mesh. Results of the harmonic mean are given in blue, with light blue being the results of the refined mesh.

other two directions is with up to 10% of the largest, numerical trends of k_{yy} and k_{zz} are closer with a maximum relative deviation of 2.5%. With regard to the numerical error, the following trends can be observed: First, the thermal conductivities resulting from the simulations based on the arithmetic mean are generally greater than those of the harmonic mean. This observation is consistent with theory (Gwanyama, 2004) and can be taken as an indication of reasonable numerics. Second, taking into account the results of the refined meshes, the impression arises that the two averaging methods converge towards a final value. The arithmetic mean has the character of an overestimator and the harmonic is mean that of an underestimator. This tendency is also largely supported by the extrapolated values, with the thermal conductivities of 4.56, 5.11 and 4.98 W m⁻¹ K⁻¹ for the arithmetic mean in the *x*, *y* and *z*-directions and 4.67, 5.10 and 4.98 W m⁻¹ K⁻¹ for the harmonic mean in the corresponding directions. The only exception occurs for the thermal conductivity in the *x*-direction. There, the extrapolated value of the arithmetic mean is lower than that of the harmonic mean. This might be an indication of insufficient mesh refinement. Third, the comparison of the averaging methods for a given direction reveals a maximum relative deviation between arithmetic and harmonic mean on the unrefined base mesh in the *x*-direction. With a value of
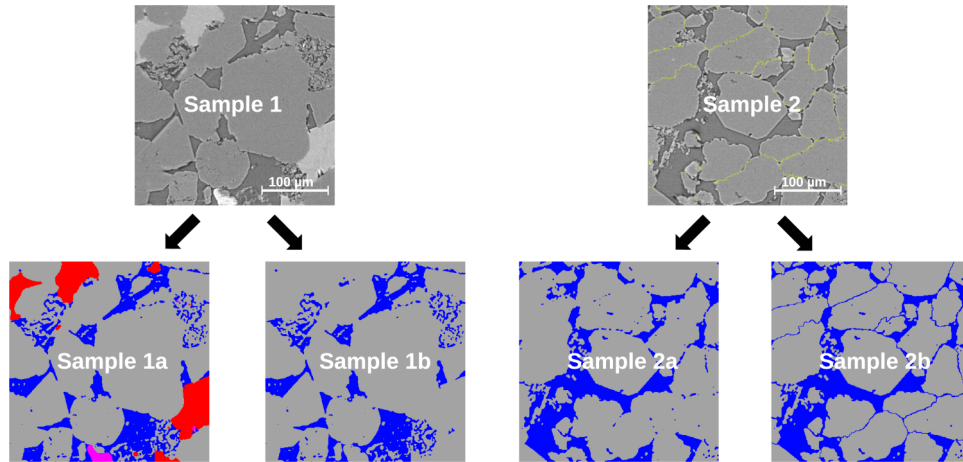
Figure 9 Two-dimensional slices of samples 1a, 1b, 2a and 2b, and blue areas represent the pore phase, grey areas the quartz phase, red areas the ankerite phase and pink areas the zircon phase.

9%, we observe that the averaging method can indeed have a strong influence on the numerical outcome. Fourth, with regard to the influence of the mesh refinement, for a given averaging method the maximum relative deviation of two successive meshes is up to 4.5%.

3.2 Influence of the sample

In the next step, the influence of individual samples on the effective thermal conductivity is investigated. In total, the results of four samples are compared. All samples are based on samples 1 and 2 presented in Section 2.1.2. By changing the thermal conductivity of the individual phases, two additional samples are generated. The overall picture is as follows:

- **Sample 1a** is equal to the original sample 1 and contains four phases. The results of this sample are already known from the previous section (Section 3.1) and are used as a reference. For all directions, voxels 301–700 of the original 1024^3 sample are used.
- **Sample 1b** is identical to the structure of sample 1a, but all mineral phases are declared as quartz. Using this sample, the influence of the ankerite and zircon phases on the total thermal conductivity can be studied.
- **Sample 2a** originates from the data of sample 2. The contact phase is assigned to the quartz phase. This sample can be used to check whether the position of the sample has an influence on the effective thermal conductivity. Based on the original 1024^3 sample, voxels 249–648 are used in the *x*-direction, 181–580 in the *y*-direction and 625–1024 in the *z*-direction.

- **Sample 2b** is based on the data of sample 2; here the contact phase is completely assigned to the pore phase. The influence of grain-to-grain contacts can thus be studied.

A graphical representation of all samples is given in Figure 9. From a numerical point of view, the same aspects as in the previous investigation are considered. That is, the directional dependence as well as the influence of the mesh resolution is studied. Extrapolated values are not determined. The results of the investigation are shown in Figure 8. Initially, the focus is shifted to the numerical error of the individual samples. While samples 1b and 2a reveal a similar trend as the already analysed sample 1a, the numerical behaviour of sample 2b shows unique features. In particular, the numerical behaviour of the arithmetic mean of the non-refined base mesh can be considered as an outlier. Whereas most numerical results of sample 2b generally underestimate the experimental value, an overestimation takes place for the arithmetic mean on the first mesh. This can be explained by considering that the contact phase in sample 2 is often only one voxel wide. Using the current material properties ($k_{air} \ll k_{quartz}$), the thermal conductivity at the interfaces between pore and mineral cells differ significantly

$$k_h = \frac{2k_{air}k_{quartz}}{k_{air} + k_{quartz}} = 0.052 \text{ W m}^{-1} \text{ K}^{-1}, \tag{5}$$

$$k_a = \frac{k_{air} + k_{quartz}}{2} = 3.858 \text{ W m}^{-1} \text{ K}^{-1}. \tag{6}$$

That is, the harmonic mean detects the isolating effect of the contact phase much better than the arithmetic mean. Only when the resolution of the contact-line is increased, in other words one numerical cell is halved in all spatial directions

during mesh refinement, the arithmetic mean starts to detect the isolating effect of the contact phase. It can be concluded that the arithmetic mean is not a good choice for low-resolution contact phases. Therefore, for further analysis of the sample influence, the results of the arithmetic mean on the first mesh of sample 2b are omitted.

In a second step of the analysis, the influence of the individual phases on the effective thermal conductivity is investigated. As can be seen in Figure 8, all samples show a slightly anisotropic character with $k_{yy} > k_{zz} > k_{xx}$. Furthermore, a clear distinction can be made between samples 1a, 1b and 2a on the one hand and sample 2b on the other. While 1a, 1b and 2a overpredict the experimental results, sample 2b underpredicts the experimental results. One reason for this might be the insufficient resolution of the tomographic dataset. As can be seen from Figure 3, the current voxel resolution of 0.74 μm only captures 85% of the pores that can be detected by mercury porosimetry. The pores that form the grain-to-grain contact are expected to have a large impact on the overall thermal conductivity. While these areas are underestimated in samples 1a, 1b and 2a, sample 2b artificially captures these areas. In fact, the results suggest that the present application of the watershed approach overestimates this effect, resulting in a thermal conductivity that is lower than that of the experimental data.

For samples 1a, 1b and 2a, the general trend $k_{1b} > k_{1a} > k_{2a}$ can be observed. The first part of this observation, namely $k_{1b} > k_{1a}$, can be explained by the choice of material properties. While sample 1b consists only of quartz and air, sample 1a consists of four phases, namely quartz, air, ankerite and zircon. Since ankerite and zircon have a lower thermal conductivity than quartz, the effective thermal conductivity should be lower. The explanation for the observation $k_{1a} > k_{2a}$ is not straightforward as both samples have slightly different origins. In general, it was observed that sample 2 has a higher porosity than sample 1 (see Table 1). Therefore, a lower effective thermal conductivity might be assumed for sample 2.

With a deviation of about 10% between samples 1b and 2a, it is evident that the positioning of the samples might play a significant role. The influence of ankerite and zircon on the effective thermal conductivity is small. This fits to their mineral composition of roughly 4.5% and 0.5%.

# 4 SIMULATION OF PRESSURE-DEPENDENT THERMAL CONDUCTIVITY

In the scope of the second main investigation, the focus is shifted to the influence of pressure on the effective thermal conductivity. All simulations are performed with sample 2 (see Fig. 9). In the first step, the approach on which the pressure-dependent simulations are based on is introduced. Afterwards, a full run of this workflow is performed. In an additional step, the influence of the proposed calibration process is analysed. Finally, the pressure-dependent thermal conductivity of the wet sample is investigated.

4.1 Pressure dependence modelling and calibration workflow

Our idea for numerically modelling the influence of pressure on the thermal conductivity of rock samples is shown in Figure 10. It is assumed that in reality an increase in pressure provokes a reorientation of the rock grains (upper half of Fig. 10, from left to right). In particular, the grains are compressed and the yellow marked interfacial volume between grains (also referred to as contact phase) is minimized. In addition, microcracks are gradually closed. Within the framework of the presented numerical approach, it is assumed that the reduction of the interfacial volume has a decisive influence on the effective thermal conductivity. This influence is modelled with the ideas presented in the lower half of Figure 10. In general, the workflow is restricted to numerical models consisting of three phases, that is pore phase, grain phase and contact phase. The pore and grain phases can be determined directly from the tomographic scan by segmentation. The contact phase is detected with the already mentioned watershed algorithm (see Section 3.2). Based on this configuration, a variety of simulations are performed. Whereas the assigned thermal conductivity of the pore and grain phase is fixed using literature values, the thermal conductivity of the contact phase is varied from simulation to simulation. In the first simulation, the contact phase thermal conductivity is set equal to that of the pores $k_{contact} = k_{pore}$ (see the bottom left image of Fig. 10). For the subsequent simulations, the thermal conductivity of the contact phase is increased step by step (see the bottom centre image of Fig. 10) until finally, in the last simulation, the thermal conductivity of the grain phase is specified $k_{contact} = k_{grain}$ (see the bottom right image of Fig. 10). The pressure effect is thus mimicked by adjusting the thermal conductivity of the contact phase. The number of simulations is user dependent. In the present work, at least 20 simulations are usually used to trace a full pressure-dependent curve.

While the effective thermal conductivity resulting from these simulations can be plotted as a function of contact phase thermal conductivity, the effective thermal conductivities of

Experiment

Simulation
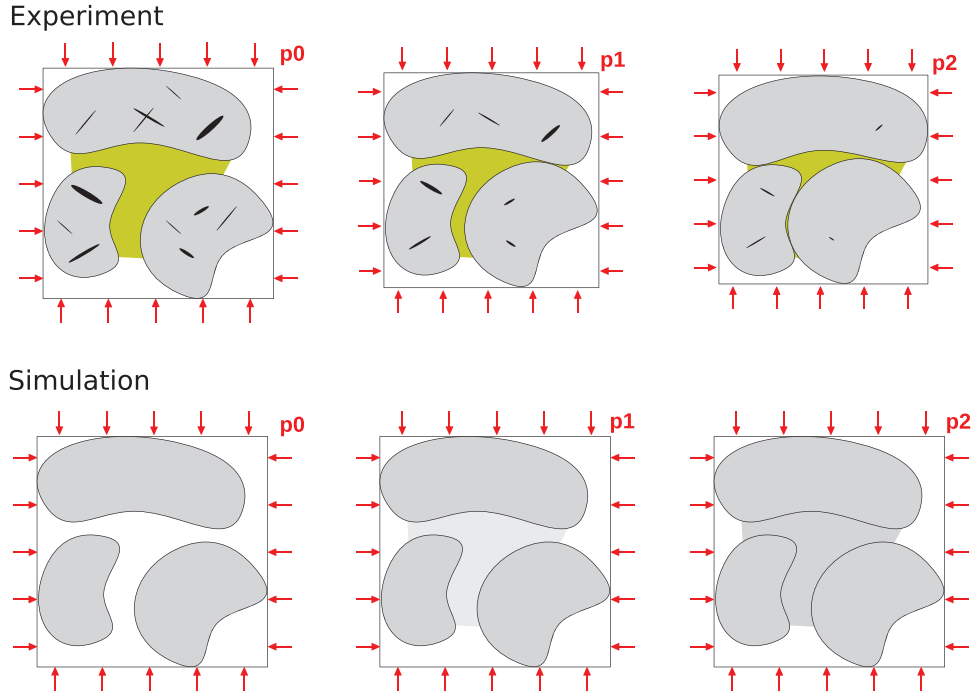
Figure 10 Top: Effect of increasing pressure ($p0 < p1 < p2$, from left to right) on the microstructure of a rock, with grey representing grains, white pore space, yellow grain contact zones and black microcracks. An increase in pressure closes the microcracks and reduces the area of the grain contact zone. Bottom: General idea on how to mimic pressure increase in our numerical model. Assigned thermal conductivity of the grain contact zone is increased during the simulation process (from left to right) in order to mimic the pressure effect.

the experimental data are given as a function of pressure. If the two datasets are to be compared, a transformation rule between pressure and contact phase thermal conductivity is required. Following the example of Quintal *et al.* (2011), Madonna *et al.* (2012) and Saenger *et al.* (2016), a linear relationship is assumed

$$k_{\text{contact}}(p) = ap + b. \tag{7}$$

To determine the two unknown quantities a and b, two pressure information from the experimental dataset are used. The minimum thermal conductivity of the contact phase $k_{\text{min}}^{(0)} = k_{\text{pore}}$ is correlated with the lower pressure p_{min}. The maximum thermal conductivity of the contact phase $k_{\text{max}}^{(0)} = k_{\text{grain}}$ is correlated with the upper pressure p_{max} (see Fig. 11). This results in

$$k_{\text{contact}}^{(0)}(p) = \frac{k_{\text{grain}} - k_{\text{pore}}}{p_{\text{max}} - p_{\text{min}}}(p - p_{\text{min}}) + k_{\text{pore}}. \tag{8}$$

As will be seen in Section 4.2, this non-calibrated approach does not necessarily result in a perfect fit between numerical and experimental data. In order to optimize this fit, a calibration workflow is introduced. The basic idea of the cali-
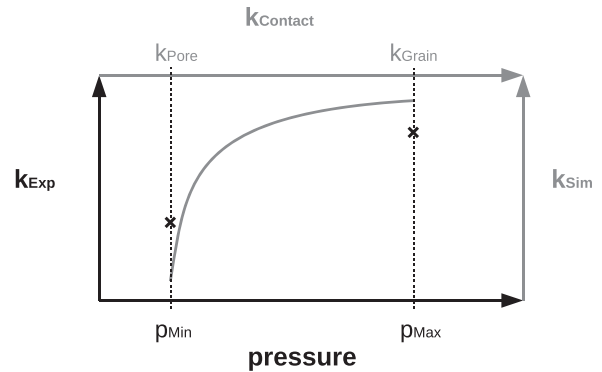
Figure 11 Setup for the non-calibrated curve; the *x*-axis of the numerical model is linearly correlated with experimentally determined pressure.

bration workflow is the adjustment of the thermal conductivity of the grain and contact phase. Here we will focus on the mathematical description of our calibration process. A visual motivated explanation is given in Appendix A. Overall, the calibration process is iterative in nature (see Fig. 12). Based on a given simulation dataset (superscript *n*), adjusted material properties for the grain phase and the contact phase
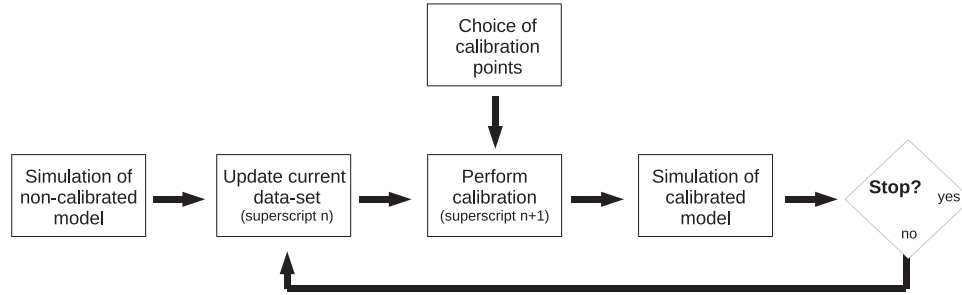
Figure 12 Flowchart of the presented calibration workflow.

(superscript $n + 1$) can be calculated as

$$k_{\text{grain}}^{(n+1)} = k_{\text{grain}}^{(n)} \frac{k_{\text{exp,max}}}{k_{\text{sim,max}}^{(n)}}, \tag{9}$$

$$k_{\text{contact}}^{(n+1)}(p) = a^{(n+1)}p + b^{(n+1)}, \tag{10}$$

with

$$a^{(n+1)} = \frac{k_{\text{contact,upper}}^{(n+1)} - k_{\text{contact,lower}}^{(n+1)}}{p_{\text{max}} - p_{\text{min}}}, \tag{11}$$

$$b^{(n+1)} = k_{\text{contact,lower}}^{(n+1)} - a p_{\text{min}}, \tag{12}$$

and

$$k_{\text{contact,upper}}^{(n+1)} = k_{\text{grain}}^{(n+1)}, \tag{13}$$

$$k_{\text{contact,lower}}^{(n+1)} = \frac{\tilde{k}_{\text{contact,NB2}}^{(n)} - \tilde{k}_{\text{contact,NB1}}^{(n)}}{\tilde{k}_{\text{sim,NB2}}^{(n)} - \tilde{k}_{\text{sim,NB1}}^{(n)}} (k_{\text{exp,min}} - \tilde{k}_{\text{sim,NB2}}^{(n)})$$
$$+ \tilde{k}_{\text{contact,NB2}}^{(n)}, \tag{14}$$

with $\tilde{k}_{\text{sim},i}$ being the simulation results of the current simulated dataset normalized by

$$\tilde{k}_{\text{sim},i}^{(n)} = k_{\text{sim},i}^{(n)} \frac{k_{\text{exp,max}}}{k_{\text{sim,max}}^{(n)}}. \tag{15}$$

The normalized simulation results $\tilde{k}_{\text{sim,NB1}}^{(n)}$ and $\tilde{k}_{\text{sim,NB2}}^{(n)}$ represent the nearest neighbours of $k_{\text{exp,min}}$

$$\tilde{k}_{\text{sim,NB1}}^{(n)} \leq k_{\text{exp,min}} \leq \tilde{k}_{\text{sim,NB2}}^{(n)}. \tag{16}$$

If no upper or lower bound exists, both bounds are set equal $\tilde{k}_{\text{sim,NB1}}^{(n)} = \tilde{k}_{\text{sim,NB2}}^{(n)}$. The values $\tilde{k}_{\text{contact,NB1}}^{(n)}$ and $\tilde{k}_{\text{contact,NB2}}^{(n)}$ are given as their corresponding contact phase values

$$\tilde{k}_{\text{contact},i}^{(n)} = \tilde{k}_{\text{contact}}^{(n)}(\tilde{k}_{\text{sim},i}^{(n)}), \tag{17}$$

whereby $\tilde{k}_{\text{contact},i}^{(n)}$ are the linear interpolated contact values between the new grain value $k_{\text{grain}}^{(n+1)}$ and the fixed pore value k_{pore}

$$\tilde{k}_{\text{contact},i}^{(n)} = \frac{k_{\text{grain}}^{(n+1)} - k_{\text{pore}}}{k_{\text{grain}}^{(n)} - k_{\text{pore}}} \left(k_{\text{contact},i}^{(n)} - k_{\text{pore}} \right) + k_{\text{pore}}. \tag{18}$$

This approach ensures that the thermal conductivity of the contact phase (see equation (10)) will always be equal or greater than that of the pore phase.

In contrast to the grain phase and contact phase, the thermal conductivity of the pore phase is held constant at $k_{\text{pore}} = k_{\text{fluid}}$ and will not change during the whole calibration process. For a better practical understanding of this workflow, a sample calculation is given in Appendix B.

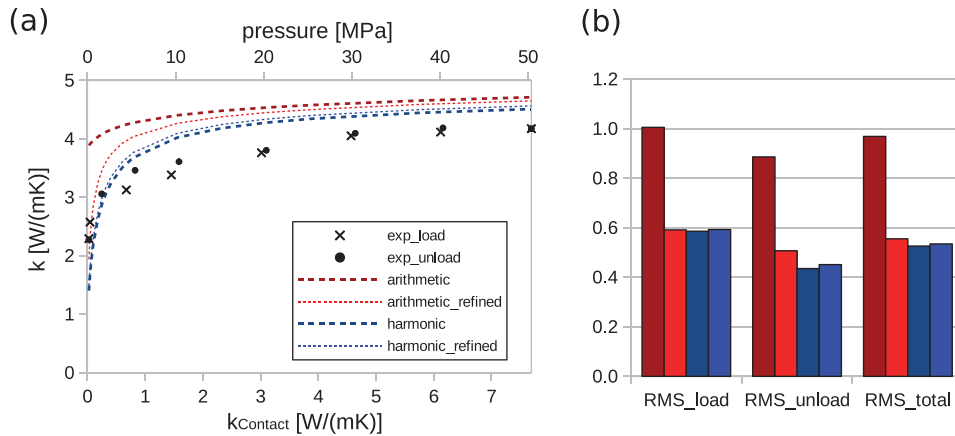### 4.2 Simulation of the non-calibrated model

In the next step, the non-calibrated curve is simulated. The pressure influence is imitated by adjusting the thermal conductivity of the contact phase. A total of 20 different values are assigned to the contact phase. All values lie in the interval between the thermal conductivities of air and quartz. The first and last simulations are carried out with the values of the associated interval limit.

In order to capture numerical errors, a mesh refinement study is performed. Both averaging methods are being used. Due to the previously observed low directional dependence, the investigation of the anisotropic behaviour is omitted. As a measure for the numerical quality, the root mean square (RMS) of the difference between numerical and experimental data is calculated

$$\text{RMS} = \sqrt{\frac{1}{n} \sum_n (k_{\text{num},i} - k_{\text{exp},i})^2}, \tag{19}$$

assuming the linear dependence between pressure and the thermal conductivity of the contact phase given by equation (8). The results of this investigation are shown in Figure 13.

As can be seen, the basic trend of the numerical and the experimental curves is similar. All curves show a steep slope at the beginning, which changes into an almost linear course with increasing pressure. The maximum thermal conductivity is well matched by all numerical curves, and the maximum relative difference is below 13%. For the classification of the minimum thermal conductivity, the already known

Figure 13 Simulation results of the non-calibrated model. Left: Pressure-dependent effective thermal conductivity; the results are mapped to the experimental data between 0.1 and 50.47 MPa. Right: RMS values of all simulation setups, divided into RMS values of the loading, unloading and total experimental curve.

trend from Section 3.2 can be observed. Whereas the arithmetic mean on the non-refined mesh overestimates the minimum experimental thermal conductivity, the remaining simulations have an underestimating character. In addition to the explanation of Section 3.2, we want to add that the underestimating character can also be interpreted physically. For the minimum pressure, the thermal conductivity of the contact phase is set to $k_{contact} = k_{air}$. In a physical sense, this means that the grains are completely isolated and virtually float in the air. In reality, contact points will always occur between the grains. We suspect that this difference between reality and numerical models can be a reason for the observed underestimation.

With regard to the influence of mesh refinement, a converging trend can generally be observed. The refinement of the mesh ensures that the differences between arithmetic and harmonic means become smaller.

Concerning the general quality of the results, the RMS values confirm the already discussed trends. Whereas the simulation results of the arithmetic mean on the unrefined mesh reveal the greatest deviations from the experimental data with RMS values of up to 1, the RMS values of the remaining simulations are all lower and on a similar level at about 0.5. Additionally, it is observed that all simulation results generally match the experimental data of the unloading curve better than those of the loading curve.

4.3 Simulation of the calibrated model

In the context of this investigation, the match between the numerical model and experimental data is optimized by using the calibration approach presented in Section 4.1. Based on the data from the previous investigation and the calibration points $P_{min}(0.1 \text{ MPa}, 2.29 \text{ W m}^{-1} \text{ K}^{-1})$ and $P_{max}(50.47 \text{ MPa}, 4.17 \text{ W m}^{-1} \text{ K}^{-1})$, a template for the material properties is developed. Specifically, calibrated thermal conductivities for the grain and contact phases are determined. The thermal conductivity of the pore phase is not changed. All simulations performed here are based on the harmonic mean and the unrefined mesh only. The calibration model has an iterative character. The results of the first three iterations are given in Table 3. A graphical representation can be found in Figure 14.

As described in Section 4.1, all templates suggest a minimum thermal conductivity of the contact phase that is greater than that of the pore phase. Figuratively speaking, the templates require that the grains do not float. This can be seen as a confirmation of the physical interpretation formulated in Section 4.2 regarding the necessity of contact points between the individual grains. Furthermore, it can be stated that all templates do not differ greatly from each other. All thermal conductivities of the grain phase are below the original quartz value and only differ slightly from each other (relative differences below 0.1%). The linear courses of the contact phase thermal conductivity are very similar as well. We, therefore, decide to use the dataset of the first iteration for further investigation. The corresponding results are given in Figure 15.

Overall, it can be stated that the calibration process improves the fit between the numerical model and the experimental data. While the non-calibrated curve has a total RMS value of 0.53, the total RMS value of the calibrated curve is only 0.15. In particular, the first and last points are very well represented by the calibrated curve, with relative differences

Table 3 Calibration templates for iterations one, two and three of the dry sample. Iteration zero is equal to the non-calibrated model. All thermal conductivities are given in unit $\mathrm{W\,m^{-1}\,K^{-1}}$

| Iteration | Pore Phase | Contact Phase | | | Grain Phase |
		Lower	Pressure Dependence	Upper	
0	0.026	0.0260	$0.1522p + 0.0108$	7.6900	7.6900
1	0.026	0.1442	$0.1384p + 0.1304$	7.1179	7.1179
2	0.026	0.1441	$0.1383p + 0.1303$	7.1111	7.1111
3	0.026	0.1441	$0.1383p + 0.1303$	7.1110	7.1110
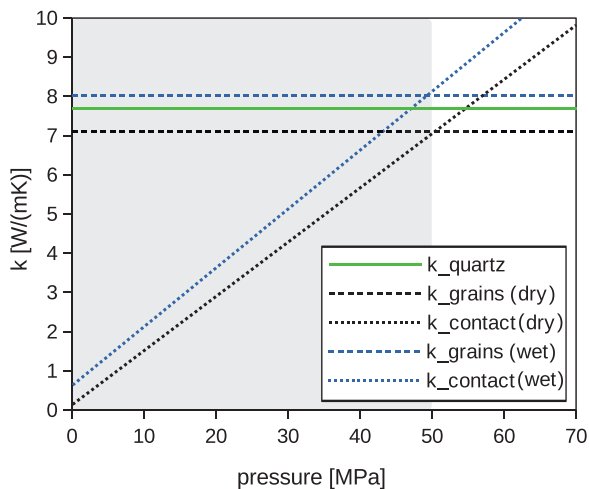
Figure 14 Graphical representation of the calibration template for the dry (black) and wet (blue) sample. Results of the second iteration are shown. Dotted lines show the suggested thermal conductivities for an optimized fit between numerical model and experimental data. The solid green line represents the literature value of quartz. The grey area marks the region between the calibration points.
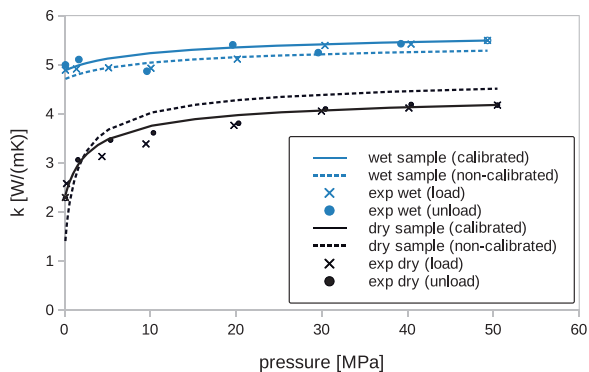
Figure 15 Simulated pressure-dependent thermal conductivity for the dry and wet model, experimental data are given as a reference. Results of the non-calibrated as well as the calibrated model are shown.

below 2%. The intermediate points can be grouped into three ranges, namely low pressure, medium pressure and high pressure. While the low- and high-pressure ranges are well captured, the results of the medium pressure range do not match as well.

In terms of the loading and unloading curves, it can be seen that the fit to the unloading curve (RMS value of 0.09) is better than the fit to the loading curve (RMS value of 0.18). Overall, the results show that the assumptions of the calibration procedure, especially the linear relation between pressure and contact phase thermal conductivity, can provide a good agreement with the experimental data. Even the results from the extrapolated range seem to give a reasonable outcome by continuing the linear trend (see Section 4.4).
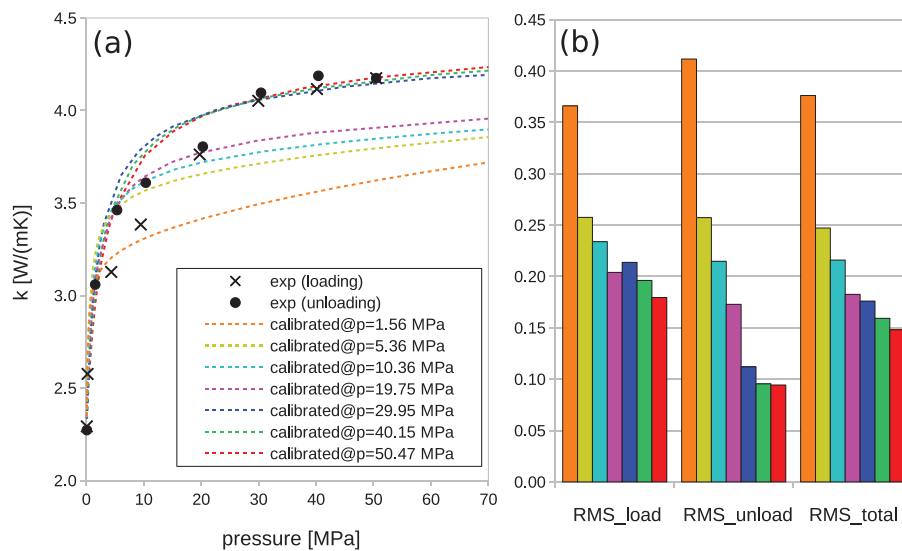
4.4 Influence of the calibration points

We have seen from the previous investigations that the calibration process seems to work well for the problem at hand. Using the non-calibrated model, as well as two calibration points, we were able to optimize the agreement between the numerical model and experimental data. Here, the focus is shifted to the choice of the calibration points and its influence on the numerical results.

When choosing the calibration points, it is taken into account that the measurement of the thermal conductivity at ambient pressure is relatively straightforward. In contrast, the choice of the maximum possible pressure will depend on the technical limitations of the measurement setup. Consequently, it is decided to fix the minimum calibration point at ambient pressure, namely $P_{\min}(0.1\ \mathrm{MPa},\ 2.29\ \mathrm{W\,m^{-1}\,K^{-1}})$. The maximum calibration point $P_{\max}$ will be varied. From a numerical point of view, simulations are again restricted to the harmonic mean and the unrefined mesh. Also, as before, the calibration model is based on the results of the first iteration. In the first step, the resulting templates are presented. A total of seven

Table 4 Calibrated models for all calibration point configurations investigated here, the minimum calibration point is fixed at P_{min}(0.1 MPa, 2.29 W m^{-1} K^{-1}), the maximum calibration point is given in columns one and two. All thermal conductivities are given in unit W m^{-1} K^{-1}. All pressures are given in unit MPa

Calibration Point			Contact Phase			
Calibration Point	k_{max}	Pore Phase	Lower	Pressure Dependence	Upper	Grain Phase
50.47	4.17	0.026	0.1442	$0.1384p + 0.1304$	7.1179	7.1179
40.15	4.12	0.026	0.1484	$0.1715p + 0.1313$	7.0182	7.0182
29.95	4.05	0.026	0.1531	$0.2263p + 0.1304$	6.9093	6.9093
19.75	3.76	0.026	0.1842	$0.3171p + 0.1525$	6.4148	6.4148
10.36	3.61	0.026	0.2034	$0.5800p + 0.1454$	6.1547	6.1547
5.36	3.46	0.026	0.2296	$1.0785p + 0.1217$	5.9026	5.9026
1.56	3.06	0.026	0.3521	$3.3316p + 0.0189$	5.2163	5.2163

Figure 16 Simulation results of all calibrated models, showing the influence of the selected calibration points: (a) plot of effective thermal conductivity vs. pressure and (b) RMS error of the individual investigations.

calibration configurations are examined. The results are shown in Table 4.

As can be seen, the thermal conductivity of the grain phase generally decreases with decreasing p_{max} values. Furthermore, the slope of the linear equation underlying the contact phase increases. In addition, it should be mentioned that all templates suggest an initial value for the thermal conductivity of the contact phases, which is greater than that of the pore phase.

Based on these templates, the numerical simulations of the calibrated curves can be carried out. For better comparability of the individual curves, all simulations are performed in the pressure range from 0.1 to 70 MPa. The results of this study are shown in Figure 16.

In general, three main tendencies can be deduced from the results. First, the higher the calibration point, the smaller the total RMS value becomes. With one exception, this behaviour is also confirmed by the RMS values of the loading and unloading curves. Regarding the course of the individual curves, we observe that higher calibration points tend to lead to better results. Second, the RMS errors of the unloading curves are generally smaller than those of the loading curve. This is convenient, since most of the lower calibration points ($p_{max} < 15$ MPa) belong to the unloading curve. Third, no matter how the calibration point is chosen, all curves are characterized by the already known course. That is, for small pressure values a steep slope arises, which changes into an almost linear course with increasing pressure.

In conclusion, the choice of calibration points can have a great influence on the quality of the results. A possible physical interpretation is given by Pimienta *et al.* (2014). In this study, Pimienta et al. investigated the pressure dependence of rock samples. In particular, they found for Berea sandstone that the transition from the steep slope to linear progression starts at a certain characteristic pressure value. From a physical point of view, they explain this behaviour with the idea that the total porosity of a rock sample is composed of two parts, namely stiff main pores and smaller and more easily deformable micropores. According to Pimienta et al., it can be assumed that in the case of the Berea sandstone, most micropores are already closed at a pressure of 30 MPa and the behaviour of the main pores dominates the effective thermal conductivity. Taking into account the results obtained here, this finding suggests that the second calibration point should ideally be placed in the area in which the micropores are already closed.

4.5 Calibration of the water-filled sample

Whereas all previous investigations refer to the experimental data of the dry sample, here the pressure-dependent thermal conductivity of the wet sample will be investigated. The complete calibration process is carried out. Starting with the simulation of the non-calibrated curve, followed by the determination of the calibration template and ending with the calibrated curve.

In the context of this investigation, simulations are restricted to the calibration points $P_{\min}$ (0.1 MPa, 4.87 W m^{-1} K^{-1}) and $P_{\max}$ (49.32 MPa, 5.49 W m^{-1} K^{-1}). From a numerical point of view, again only the harmonic mean and the non-refined mesh are used. Directional dependencies are not investigated. In general, it should be noted that for the simulation of the wet sample the thermal conductivity of the pore phase has to be adjusted. Hence, the thermal conductivity of water is assigned. The results of the non-calibrated curve are shown in Figure 15. As a reference, the data of the dry sample are plotted as well.

Already without making use of the proposed calibration process, very good results can be obtained. In particular, the two limits of the measurement interval are already hit well with a relative difference of below 4%. In addition, it becomes clear that the basic course of the wet sample is similar to that of the dry sample. For low-pressure values, a strong gradient occurs that continuously decreases and finally leads to a linear course. In direct comparison, however, it is clear that the gradient is much less pronounced than that of the dry sample.

Based on this dataset, the calibration template is created. The results of iterations one to three are shown in Table 5. A graphical representation can be found in Figure 14. As can be seen, within the first iteration the template predicts a minimum contact phase value that is identical to that of the pore phase $k_{\text{contact,lower}} = k_{\text{pore}}$. Considering the previously used interpretation logic of Section 4.3, this behaviour can be considered non-physical. Consequently, iterations two and three are performed. Resulting in a contact phase thermal conductivity that is slightly higher than that of the pore phase and therefore fulfills the physical intuition of non-floating grains. In addition, it should be mentioned that the thermal conductivity of the grain phase is above that of quartz. In the preceding investigation (see Table 4), the opposite trend can be observed.

The results of the calibrated curve of the second iteration are shown in Figure 15. As a reference, the results of the dry sample are given as well. Overall, the result of the calibrated curve is convincing. However, due to the already very high quality of the non-calibrated dataset, the improvement is only marginal with a decrease in the total RMS value by 0.02. In contrast, the calibration process of the dry sample reveals a much greater improvement with respect to the non-calibrated curve, with an RMS value of 0.53 before calibration and a RMS value of 0.15 after calibration. Furthermore, it can be seen that the agreement between the calibrated curve and the experimental data in the intermediate pressure range from 10 to 30 MPa is not good. However, in this range, the quality of the measurement should also be questioned. For example, the measured thermal conductivity of 5 MPa is higher than that of 10 MPa. With regard to the before observed trends, this behaviour seems at least questionable. Finally, it should be mentioned that the RMS values of the loading and unloading curves are very similar with approximately 0.15.

Overall, the presented calibration process shows good agreement with the experimental data and thus confirms the already observed trend for the dry sample.

5 DISCUSSION

Based on the example of Berea sandstone, it is shown how pressure-dependent effective thermal conductivity of rock samples can be simulated using the methods of digital rock physics. On the basis of a given tomographic scan (Madonna *et al.*, 2013), four segmented subsamples are created. These subsamples can generally be divided into two groups (see Fig. 9). While the subsamples of the first group are directly derived from the segmented tomographic scan, the second group is characterized by an additional

Table 5 Calibration templates for iterations one, two and three of the wet sample. Iteration zero is equal to the non-calibrated model. All thermal conductivities are given in unit W m^{-1} K^{-1}. All pressures are given in unit MPa

| Iteration | Pore Phase | Contact Phase | | | Grain Phase |
		Lower	Pressure Dependence	Upper	
0	0.61	0.6100	$0.1522p + 0.0108$	7.6900	7.6900
1	0.61	0.6100	$0.1500p + 0.5950$	7.9933	7.9933
2	0.61	0.6385	$0.1501p + 0.6235$	8.0259	8.0259
3	0.61	0.6429	$0.1501p + 0.6279$	8.0294	8.0294

artificial reconstruction of the grain boundaries using the watershed algorithm. Two main questions are investigated: First, how well do the samples represent the effective thermal conductivity under ambient conditions? And second, how can pressure-dependent thermal conductivity be modelled? All results are validated with the experimental data of Lin *et al.* (2011).

With regard to the first question, it is observed that the simulation results of the non-manipulated subsamples (first group) generally deviate strongly from the measured thermal conductivities. Only when taking into account the artificially modelled grain boundaries (second group), a thermal conductivity close to that of the experimental data was obtained. In particular, the following tendency is observed: While the non-manipulated samples generally overestimate the findings of the experimental data, the manipulated sample results in a simulated thermal conductivity that is too low. As a possible explanation, it is assumed that the given resolution of the investigated rock sample is not sufficient to represent all essential structures (e.g. grain boundaries) for the numerical modelling of effective thermal conductivity. Furthermore, the fact that the numerical model has a different origin than the sample of experimental data should be considered as another source of error.

With regard to the second question, it is observed that derived workflow provides satisfactory results. Good agreement between simulation and experimental data is obtained for both dry and wet samples. Especially, the proposed linear correlation between the thermal conductivity of the contact phase and experimentally measured pressure leads to reasonable results. Regarding the choice of calibration points, it is observed that the second calibration point should optimally be placed in the region that is weakly dependent on pressure, here $p \geq 30$ MPa. For a classification of our results, we refer to Saenger *et al.* (2016). Saenger et al. carried out a similar workflow for the numerical determination of elasticity in rock samples and found analogous trends. The fact that pressure-dependent thermal conductivity and elasticity behave likewise
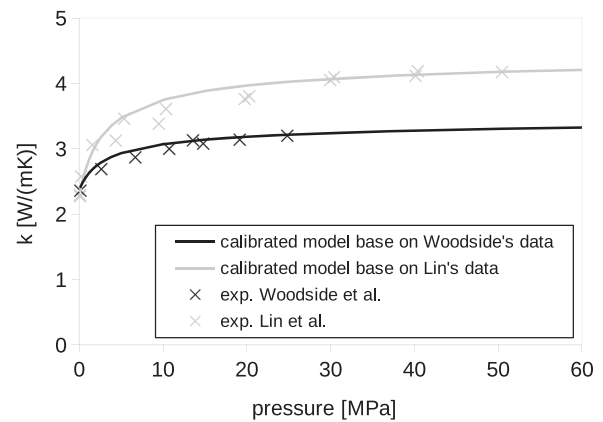

Figure 17 Pressure-dependent thermal conductivity, calibrations are based on two different experimental datasets (Woodside and Messmer, 1961; Lin *et al.*, 2011).

in the case of Berea sandstone was also noted by Pimienta *et al.* (2014).

With regard to future investigations, we refer to Figure 17. Starting from the non-calibrated model created in the present work, an additional calibration using the experimental data published by Woodside and Messmer (1961) is performed. While these data were also recorded for Berea sandstone and the corresponding porosity is relatively similar to that of Lin *et al.* (2011), with $\phi_{\text{Woodside}} = 22\%$ and $\phi_{\text{Lin}} = 19.7\%$, experimental results differ significantly from each other. Neglecting possible measurement errors, this behaviour suggests that the microstructures of the two samples are different. Despite these variations, the calibrated models show very good agreement with both datasets. This indicates that the here developed model has a certain generality for the pressure-dependent thermal conductivity of Berea sandstone. Further investigations should examine to what extent these models can be generally applied to arbitrary datasets.

Another point that should be questioned is the application of the watershed algorithm for modelling grain boundaries. In general, due to the manual inputs that have to be made
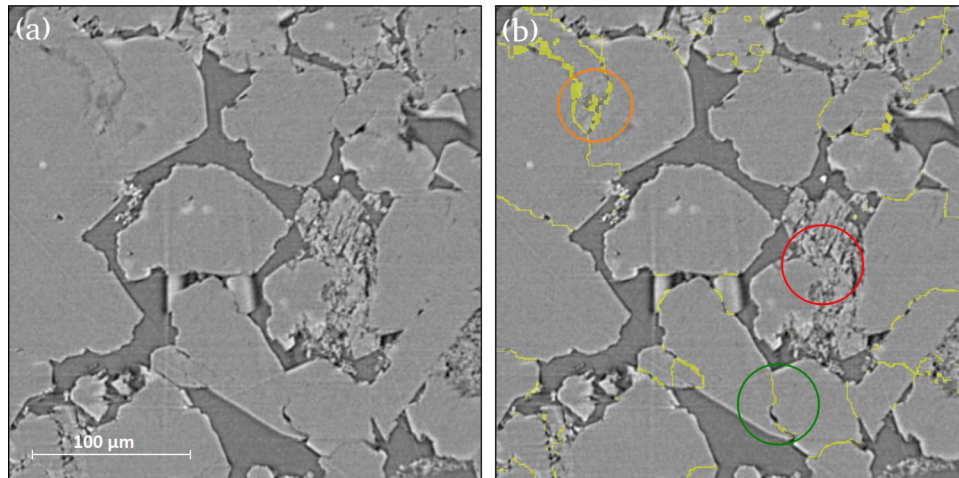
Figure 18 Typical result of the grain-to-grain contact reconstruction, original greyscale image on the left, artificially determined grain-to-grain contact (yellow lines) on the right. Circles mark examples of the reconstruction quality. The green circle as an example for a very good reconstruction of the contact zone, orange circle as an example for a reconstruction with artifacts and red circle as an example of the non-existent reconstruction for cracked grains.

during the watershed algorithm (e.g. placing markers) the objectivity and reproducibility of the grain boundary modelling is questionable and should be investigated more closely (see Fig. 18). In this regard, future investigations might also include a detailed analysis of the representative elementary volume.

6 CONCLUSION

A new workflow for determining the pressure-dependent thermal conductivity of rock samples was developed. Using the approach of digital rock physics as a starting point, the workflow was tested for a given tomographic scan of Berea sandstone. As a first investigation, the capabilities of the derived numerical models are tested by performing simulations under ambient conditions. It is observed that all numerical models overpredict the experimentally measured data by a factor of roughly two. This behaviour is attributed to the resolution of the scan. Concluding that the resolution of the tomographic scan is too low to correctly represent all structures influencing the effective thermal conductivity. In particular, it is assumed that the insulating boundaries between individual grains are not captured with sufficient accuracy. To test this hypothesis, the grain boundaries were artificially reconstructed and added to an additional model. The results of this new model show a better fit to the experimental data.

Building on these results, the proposed workflow for the determination of the pressure-dependent thermal conductivity in rock samples is introduced. Starting from the numerical model with reconstructed grain boundaries, the influence of pressure is represented by an adjustment of the thermal conductivity in the grain boundary regions. As a direct translation rule, a linear dependence between the adjusted thermal conductivity of the grain boundaries and experimentally measured pressure values is used. Following this approach, it is observed that the numerical results do generally reflect basic trends of experimental data. In order to improve the fit further, a calibration workflow is presented and tested. In general, the results show that the application of the proposed workflow leads to an optimized fit for all investigated configurations.

DATA AVAILABILITY STATEMENT

The tomographic scan of the Berea sandstone sample used in the current study can be found at https://www.rockphysics.org/index.php/downloads, Madonna *et al.* (2013). All segmented samples will be made available on request. The source code of the numerical solver and additional tools will be made available on request.

ORCID

Mirko Siegert (iD) https://orcid.org/0000-0002-6704-4935
Marcel Gurris (iD) https://orcid.org/0000-0001-5243-1038
Claudia Finger (iD) https://orcid.org/0000-0003-2151-5460
Erik H. Saenger (iD) https://orcid.org/0000-0002-2057-4728

REFERENCES

Abdulagatov, I.M., Emirov, S.N., Abdulagatova, Z.Z. and Askerov, S.Y. (2006) Effect of pressure and temperature on the thermal conductivity of rocks. *Journal of Chemical & Engineering Data*, 51, 22–33. https://doi.org/10.1021/je050016a.

Beck, A., Darbha, D. and Schloessin, H. (1978) Lattice conductivities of single-crystal and polycrystalline materials at mantle pressures and temperatures. *Physics of the Earth and Planetary Interiors*, 17, 35–53. https://doi.org/10.1016/0031-9201(78)90008-0.

Beucher, S. and Meyer, F. (2018) The Morphological Approach to Segmentation: The Watershed Transformation. *Mathematical Morphology in Image Processing*, CRC Press, 433–481. https://doi.org/10.1201/9781482277234-12

Birch, F. and Clark, H. (1940) The thermal conductivity of rocks and its dependence upon temperature and composition. *American Journal of Science*, 238, 529–558. https://doi.org/10.2475/ajs.238.8.529.

Blackwell, D.D. and Steele, J.L. (1989) Thermal conductivity of sedimentary rocks: measurement and significance. In: Naeser, N.D. and McCulloh, T.H. (Eds.) *Thermal History of Sedimentary Basins*. Springer New York. pp. 13–36. https://doi.org/10.1007/978-1-4612-3492-0_2.

Cermak, V. and Rybach, L. (1982) Thermal conductivity and specific heat of minerals and rocks. In: Beblo, M. (Ed.) *Landolt-Börnstein: Numerical Data and Functional Relationships in Science and Technology, New Series, Group V (Geophysics and Space Research), Vol. 1a (Physical Properties of Rocks)*. Springer-Verlag. pp. 305–343.

Chekhonin, E., Popov, Y., Peshkov, G., Spasennykh, M., Popov, E. and Romushkevich, R. (2019) On the importance of rock thermal conductivity and heat flow density in basin and petroleum system modelling. *Basin Research*, 32, 1261–1276. https://doi.org/10.1111/bre.12427.

Clauser, C. and Huenges, E. (2013) Thermal conductivity of rocks and minerals. In: *AGU Reference Shelf*. American Geophysical Union. pp. 105–126. https://doi.org/10.1029/rf003p0105.

Desai, P., Navarro, R., Hasan, S. and Ho, C. (1974) *Thermophysical Properties of Selected Rocks*. CINDAS report. Center for Information and Numerical Data Analysis and Synthesis, Purdue University.

Do, D.P. and Hoxha, D. (2013) Temperature and pressure dependence of the effective thermal conductivity of geomaterials: numerical investigation by the immersed interface method. *Journal of Applied Mathematics*, 2013, 1–13. https://doi.org/10.1155/2013/456931.

Eucken, A. (1911) Über die Temperaturabhängigkeit der Wärmeleitfähigkeit fester Nichtmetalle. *Annalen der Physik*, 339, 185–221. https://doi.org/10.1002/andp.19113390202.

Fourier, J. (1822) *Théorie analytique de la chaleur*. F. Didot.

Gwanyama, P.W. (2004) The HM-GM-AM-QM inequalities. *The College Mathematics Journal*, 35, 47. https://doi.org/10.2307/4146884.

Hestenes, M. and Stiefel, E. (1952) Methods of conjugate gradients for solving linear systems. *Journal of Research of the National Bureau of Standards*, 49, 409. https://doi.org/10.6028/jres.049.044.

Hicks, P.J., Fraticelli, C.M., Hardy, M.J., Shosa, J.D. and Townsley, M.B. (2012) Identifying and quantifying significant uncertainties in basin modeling. In: Peters, K.E., Curry, D.J. and Kacewicz, M. (Eds.) *Basin Modeling: New Horizons in Research and Applications*. American Association of Petroleum Geologists. pp. 207–219. https://doi.org/10.1306/13311437H41527.

Horai, K. (1971) Thermal conductivity of rock-forming minerals. *Journal of Geophysical Research*, 76, 1278–1308. https://doi.org/10.1029/jb076i005p01278.

Horai, K. and Simmons, G. (1969) Thermal conductivity of rock-forming minerals. *Earth and Planetary Science Letters*, 6, 359–368. https://doi.org/10.1016/0012-821x(69)90186-1.

Jones, F.W. and Pascal, F. (1995) Numerical calculations of the thermal conductivities of composites—a 3-D model. *Geophysics*, 60, 1038–1050. https://doi.org/10.1190/1.1443832.

Kadioglu, S.Y., Nourgaliev, R.R. and Mousseau, V.A. (2008) *A comparative study of the harmonic and arithmetic averaging of diffusion coefficients for non-linear heat conduction problems*. Idaho National Laboratory, Idaho Falls, ID, USA. Technical Report. https://doi.org/10.2172/928087.

Kanamori, H., Fujii, N. and Mizutani, H. (1968) Thermal diffusivity measurement of rock-forming minerals from 300° to 1100°k. *Journal of Geophysical Research*, 73, 595–605. https://doi.org/10.1029/jb073i002p00595.

Legland, D., Arganda-Carreras, I. and Andrey, P. (2016) MorphoLibJ: integrated library and plugins for mathematical morphology with ImageJ. *Bioinformatics*, 32, 3532–3534. https://doi.org/10.1093/bioinformatics/btw413.

Lin, W., Tadai, O., Hirose, T., Tanikawa, W., Takahashi, M., Mukoyoshi, H. and Kinoshita, M. (2011) Thermal conductivities under high pressure in core samples from IODP NanTroSEIZE drilling site c0001. *Geochemistry, Geophysics, Geosystems*, 12, Q0AD14. https://doi.org/10.1029/2010gc003449.

Liu, Z. and Ma, C. (2005) A new method for numerical treatment of diffusion coefficients at control-volume surfaces. *Numerical Heat Transfer, Part B: Fundamentals*, 47, 491–505. https://doi.org/10.1080/10407790590919225.

Lowrie, W. and Fichtner, A. (2020) *Fundamentals of Geophysics*. Cambridge University Press. https://doi.org/10.1017/9781108685917.

MacKinnon, R. and Carey, G. (1988) Analysis of material interface discontinuities and superconvergent fluxes in finite difference theory. *Journal of Computational Physics*, 75, 151–167. https://doi.org/10.1016/0021-9991(88)90104-0.

Maddix, D.C., Sampaio, L. and Gerritsen, M. (2018) Numerical artifacts in the generalized porous medium equation: why harmonic averaging itself is not to blame. *Journal of Computational Physics*, 361, 280–298. https://doi.org/10.1016/j.jcp.2018.02.010.

Madonna, C., Almqvist, B.S. and Saenger, E.H. (2012) Digital rock physics: numerical prediction of pressure-dependent ultrasonic

velocities using micro-CT imaging. *Geophysical Journal International*, 189, 1475–1482. https://doi.org/10.1111/j.1365-246x.2012.05437.x.

Madonna, C., Quintal, B., Frehner, M., Almqvist, B.S.G., Tisato, N., Pistone, M., Marone, F. and Saenger, E.H. (2013) Synchrotron-based x-ray tomographic microscopy for rock physics investigations. *Geophysics*, 78, D53–D64. https://doi.org/10.1190/geo2012-0113.1.

Mirkovich, V.V. and Soles, J.A. (1978) Thermal conductivity of certain rock types and its relevance to the storage of nuclear waste. In: Mirkovich, V.V. (Ed.) *Thermal Conductivity 15*. Springer US. pp. 297–304. https://doi.org/10.1007/978-1-4615-9083-5_36.

Object Research Systems. (2020) *Dragonfly 2020.1.1.809*. Montreal, Canada: Object Research Systems.

Patankar, S. (1980) *Numerical Heat Transfer and Fluid Flow*. Electro Skills Series. Hemisphere Publishing.

Petrasch, J., Schrader, B., Wyss, P. and Steinfeld, A. (2008) Tomography-based determination of the effective thermal conductivity of fluid-saturated reticulate porous ceramics. *Journal of Heat Transfer*, 130, 032602. https://doi.org/10.1115/1.2804932.

Pimienta, L., Sarout, J., Esteban, L., David, C. and Clennell, M.B. (2017) Pressure-dependent elastic and transport properties of porous and permeable rocks: microstructural control. *Journal of Geophysical Research: Solid Earth*, 122, 8952–8968. https://doi.org/10.1002/2017jb014464.

Pimienta, L., Sarout, J., Esteban, L. and Piane, C.D. (2014) Prediction of rocks thermal conductivity from elastic wave velocities, mineralogy and microstructure. *Geophysical Journal International*, 197, 860–874. https://doi.org/10.1093/gji/ggu034.

Pribnow, D. and Umsonst, T. (1993) Estimation of thermal conductivity from the mineral composition: Influence of fabric and anisotropy. *Geophysical Research Letters*, 20, 2199–2202. https://doi.org/10.1029/93gl02135.

Qin, X., Cai, J., Zhou, Y. and Kang, Z. (2020) Lattice boltzmann simulation and fractal analysis of effective thermal conductivity in porous media. *Applied Thermal Engineering*, 180, 115562. https://doi.org/10.1016/j.applthermaleng.2020.115562.

Quintal, B., Frehner, M., Madonna, C., Tisato, N., Kuteynikova, M. and Saenger, E.H. (2011) Integrated numerical and laboratory rock physics applied to seismic characterization of reservoir rocks. *The Leading Edge*, 30, 1360–1367. https://doi.org/10.1190/1.3672480.

Roache, P.J. (1997) quantification of uncertainty in computational fluid dynamics. *Annual Review of Fluid Mechanics*, 29, 123–160. https://doi.org/10.1146/annurev.fluid.29.1.123.

Saenger, E.H., Lebedev, M., Uribe, D., Osorno, M., Vialle, S., Duda, M., Iglauer, S. and Steeb, H. (2016) Analysis of high-resolution x-ray computed tomography images of bentheim sandstone under elevated confining pressures. *Geophysical Prospecting*, 64, 848–859. https://doi.org/10.1111/1365-2478.12400.

Siegert, M., Gurris, M. and Saenger, E.H. (2021) Validation suite for numerical solvers calculating effective thermal conductivity in porous media. *Journal of Applied Geophysics*, 189, 104323. https://doi.org/10.1016/j.jappgeo.2021.104323.

Sipio, E.D., Chiesa, S., Destro, E., Galgaro, A., Giaretta, A., Gola, G. and Manzella, A. (2013) Rock thermal conductivity as key param-

eter for geothermal numerical models. *Energy Procedia*, 40, 87–94. https://doi.org/10.1016/j.egypro.2013.08.011.

Span, R. (2013) Stoffwerte von Luft. In: Verein Deutscher Ingenieure VDI-Gesellschaft Verfahrenstechnik und Chemieingenieurwesen (GVC) (Eds) *VDI-Wärmeatlas*. Springer Berlin Heidelberg. pp. 196–217. https://doi.org/10.1007/978-3-540-32218-4_12.

Tiab, D. and Donaldson, E.C. (2016) Introduction to petroleum geology. In: *Petrophysics*. Elsevier. pp. 23–66. https://doi.org/10.1016/b978-0-12-803188-9.00002-4.

Wagner, W. and Kretzschmar, H.-J. (2013) Stoffwerte von Wasser. In: *VDI-Wärmeatlas*. Springer Berlin Heidelberg. pp. 175–195. https://doi.org/10.1007/978-3-540-32218-4_11.

Wang, M. and Pan, N. (2008) Predictions of effective physical properties of complex multiphase materials. *Materials Science and Engineering: R: Reports*, 63, 1–30. https://doi.org/10.1016/j.mser.2008.07.001.

Woodside, W. and Messmer, J.H. (1961) Thermal conductivity of porous media. II. Consolidated rocks. *Journal of Applied Physics*, 32, 1699–1706. https://doi.org/10.1063/1.1728420.

Yang, H., Zhang, L., Liu, R., Wen, X., Yang, Y., Zhang, L., Zhang, K. and Askari, R. (2019) Thermal conduction simulation based on reconstructed digital rocks with respect to fractures. *Energies*, 12, 2768. https://doi.org/10.3390/en12142768.

APPENDIX A: VISUAL EXPLANATION OF THE PRESENT CALIBRATION WORKFLOW

Generally, the present calibration workflow is based on the following four requirements:

1. A linear dependence between the thermal conductivity of the contact phase and the experimentally determined pressure is assumed for the translation of the numerical results and the experimental data.

2. The thermal conductivity of the pore phase is constant and will not be adjusted. The thermal conductivity of the grain phase may be adjusted and is independent of the pressure. The thermal conductivity of the contact phase may be adjusted and lies between those of the pore and grain phase.

3. For mapping the second calibration point, the thermal conductivity of the contact phase shall be identical to that of the grain phase.

4. The thermal conductivity of the contact phase shall be equal to or greater than that of the pore phase.

These demands are represented by the equations of the calibration workflow given in Section 4.1. Here we want to visually explain the general ideas.

In the first step, it is assumed that the simulated maximum thermal conductivity does not match with the data of the upper calibration point $k_{\text{sim,max}} \neq k_{\text{exp,max}}$. To minimize this deviation, according to equation (15), a uniform scaling of the numerical results is performed (see the first row of
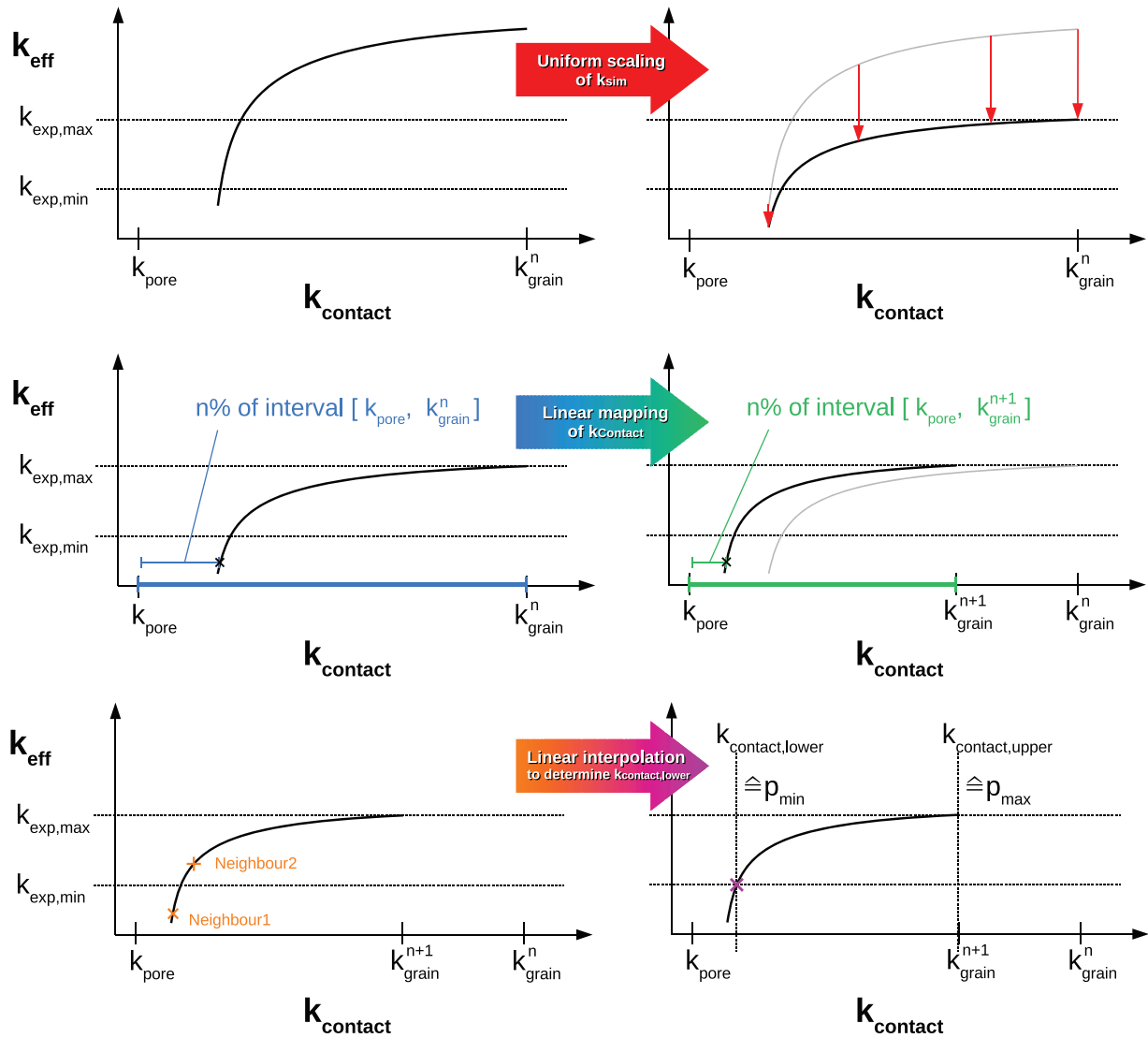
Figure A1 Visualization of the presented calibration workflow: first step of uniform scaling is given in row one, second step of linear mapping is given in the second row, third and fourth steps of linear interpolation and correlation of the experimental pressure with the numerical contact phase thermal conductivity is given in the third row. Former states are represented by grey lines.

Figure A1). It is assumed that this value can be achieved, if the thermal conductivity of the grain phase is scaled accordingly at the beginning of the simulation (see equation (9)). Whereas the thermal conductivity of the pore phase is not allowed to be manipulated in compliance with requirement 2, the thermal conductivity of the contact phase has to be adjusted under consideration of requirement 3. Additionally, in order to maintain requirement 4, a linear mapping in the abscissa direction is carried out. Following equation (18), the contact phase data originally lying between k_{pore} and k_{grain}^n are interpolated to the new boundaries k_{pore} and k_{grain}^{n+1} (see the second row of

Figure A1). The resulting datasets $\tilde{k}_{sim}^{(n)}$ and $\tilde{k}_{contact}^{(n)}$ represent an estimate for the simulation results achievable with the calibrated model. They can be used to determine the lower limit of the necessary contact phase thermal conductivity. According to equation (14), this value is linearly interpolated from the nearest neighbours of the thermal conductivity of the lower calibration point. In a final step, as specified by requirement 1, the minimum and maximum thermal conductivities of the contact phase are correlated with the pressures of both calibration points via the linear relationship (10) (see the third row of Figure A1).
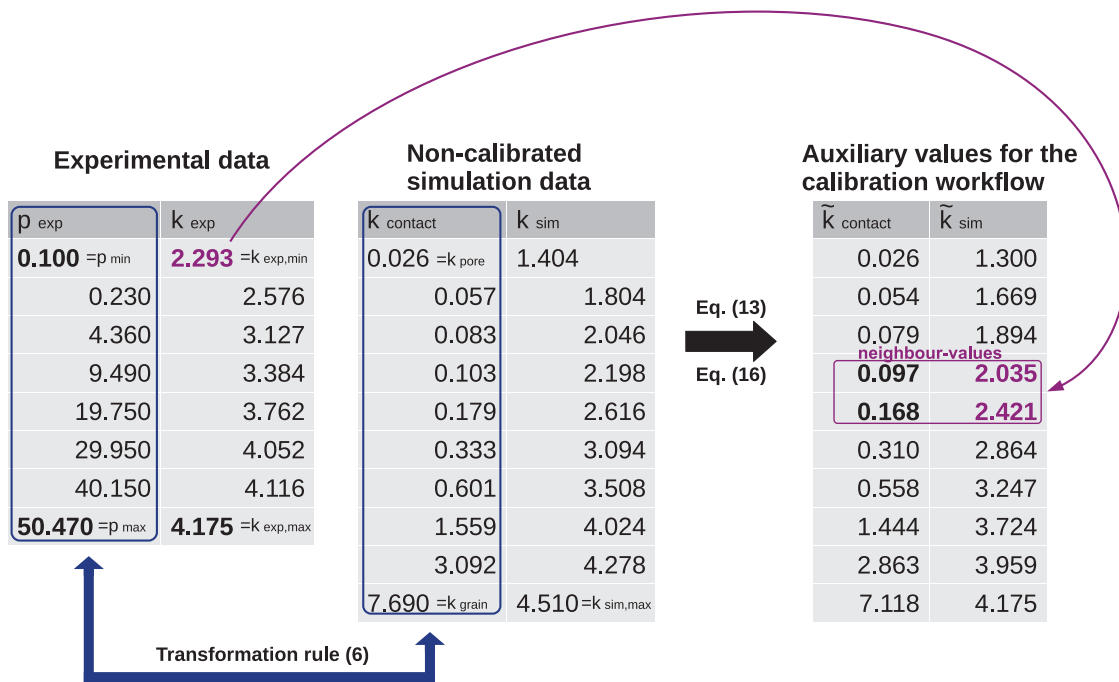
Figure B1 Calculation example of the calibration workflow, presented data are based on the simulation of the dry sample.

Experimental data		Non-calibrated simulation data			Auxiliary values for the calibration workflow	
p_{exp}	k_{exp}	$k_{contact}$	k_{sim}		$\tilde{k}_{contact}$	$\tilde{k}_{sim}$
0.100 $=p_{min}$	**2.293** $=k_{exp,min}$	0.026 $=k_{pore}$	1.404		0.026	1.300
0.230	2.576	0.057	1.804	Eq. (13)	0.054	1.669
4.360	3.127	0.083	2.046		0.079	1.894
9.490	3.384	0.103	2.198	Eq. (16)	**0.097**	**2.035**
19.750	3.762	0.179	2.616		**0.168**	**2.421**
29.950	4.052	0.333	3.094		0.310	2.864
40.150	4.116	0.601	3.508		0.558	3.247
50.470 $=p_{max}$	**4.175** $=k_{exp,max}$	1.559	4.024		1.444	3.724
		3.092	4.278		2.863	3.959
		7.690 $=k_{grain}$	4.510 $=k_{sim,max}$		7.118	4.175

neighbour-values

Transformation rule (6)

APPENDIX B: CALCULATION EXAMPLE FOR THE PRESENT CALIBRATION WORKFLOW

For a better understanding of the presented workflow for the determination of the pressure-dependent thermal conductivity (see Section 4.1), a calculation example is given below. The example is based on the setup from Section 4.2.

To determine the non-calibrated curve, the thermal conductivity of the grain and pore phase is set to the given literature values, that is $k_{grain} = 7.69$ Wm^{-1}K^{-1}, and $k_{pore} = 0.026$ Wm^{-1}K^{-1}. According to the requirements discussed in Section 4.1, the thermal conductivity of the contact phase is therefore limited by $k_{contact} \in [0.026, 7.69]$Wm^{-1}K^{-1}. Here, a total of 10 simulations with gradually increased contact phase thermal conductivities are performed. The results are shown in Figure B1. The two pressure information, necessary for comparability between numerical and experimental data are set to $p_{min} = 0.1$MPa and $p_{max} = 50.47$MPa. Using equation (8), we thus obtain the following transformation rule $k_{contact}^{(0)}(p) = 0.152p + 0.011$. A graphical representation of this result is shown in Figure 15.

In order to optimize the agreement, the calibration step can be performed. As calibration points the experimental values of p_{min} and p_{max} are used, that is $k_{exp,min} = 2.293$ W m^{-1} K^{-1} and $k_{exp,max} = 4.175$ W m^{-1} K^{-1}. Based on these data, the required adjustments to the thermal conductivity of the grain and contact phase has to be calculated. The determination of the new thermal conductivity of the grain phase is performed by using equation (9) and results in $k_{grain}^{(1)} = 7.118$ W m^{-1} K^{-1}. The computation of the new transformation rule (see equation (10)) is more complex. First, auxiliary values are computed using equations (15) and (18) (see the right-side table of Figure B1). Then, the nearest neighbours of $k_{exp,min}$ are taken according to requirement (16), in our case $\tilde{k}_{sim,NB1}^{(0)} = 2.035$ W m^{-1} K^{-1} and $\tilde{k}_{sim,NB2}^{(0)} = 2.421$ W m^{-1} K^{-1}. The corresponding contact phase values result in $\tilde{k}_{contact,NB1}^{(0)} = 0.097$ W m^{-1} K^{-1} and $\tilde{k}_{contact,NB2}^{(0)} = 0.168$ W m^{-1} K^{-1} (see equation (17)). Using these neighbour values, one can now determine $k_{contact,lower}^{(1)} = 0.144$W m^{-1} K^{-1} and $k_{contact,upper}^{(1)} = 7.118$ W m^{-1} K^{-1} (see equations (13) and (14)). With these two values, the quantities $a^{(1)}$ and $b^{(1)}$ are determined according to equations (11) and (12). The calibrated dependence between contact phase thermal conductivity and pressure is obtained from equation (10), resulting in $k_{contact}^{(1)}(p) = 0.138p + 0.130$. With this new transformation rule, as well as the adjusted thermal conductivity of the grain phase, the simulation of the calibrated curve can be performed. By repeatedly applying this workflow, the agreement between the numerical model and experimental data can further be optimized.